RSC Advances

Graphical Abstract

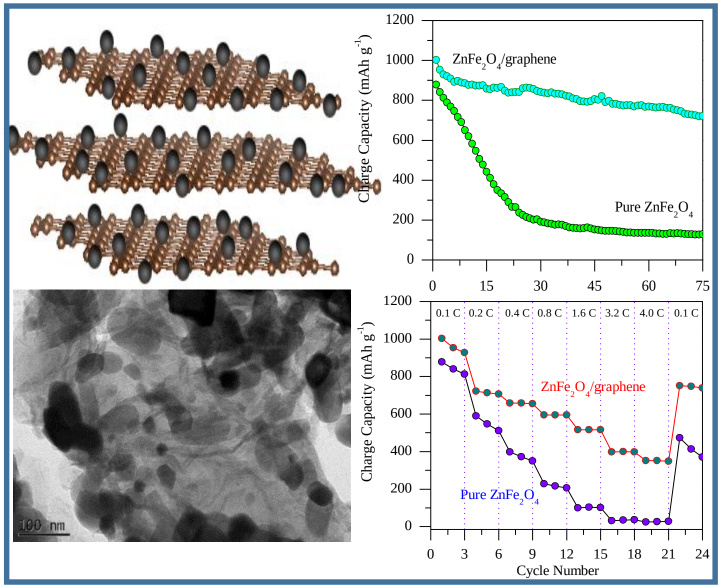

Cite this: DOI: 10.1039/c0xx00000x

www.rsc.org/xxxxxx

ARTICLE TYPE

Electrochemical Lithium Storage of $ZnFe_2O_4$/graphene Nanocomposite as an Anode Material for Rechargeable Lithium Ion Batteries

Alok Kumar Rai, Sungjin Kim, Jihyeon Gim, Muhammad Hilmy Alfaruqi, Vinod Mathew and Jaekook Kim*

Received (in XXX, XXX) Xth XXXXXXXXX 20XX, Accepted Xth XXXXXXXXX 20XX
DOI: 10.1039/b000000x

In the present work, graphene-based $ZnFe_2O_4$ nanocomposite have been synthesized using urea-assisted auto combustion synthesis followed by an annealing step. Urea synthesis is attractive, as it can rapidly synthesize materials with a high degree of control of particle size and morphology at low cost. The microstructure images clearly show that the $ZnFe_2O_4$ nanoparticles are homogeneously anchored on the surface of the graphene nanosheets. The average nanoparticle size ranges from 25−50 nm for both samples. As anode materials for lithium ion batteries, the obtained nanocomposite electrode shows significantly improved lithium storage properties with a high reversible capacity, excellent cycling stability and higher rate capability compared to pure $ZnFe_2O_4$ nanoparticle electrode. The enhanced electrochemical performance of the nanocomposite sample can be attributed to the synergistic interaction between the uniformly dispersed $ZnFe_2O_4$ nanoparticles and the graphene nanosheets, which offers a large number of accessible active sites for the fast diffusion of Li^+ ions, low internal resistance and more importantly accommodates the large volume expansion/contraction during cycling.

1. Introduction

Among various types of lithium ion battery anodes, transition metal oxides have received considerable attention, as they can achieve high capacity in the range of ~400−1000 mAh g^{-1}, which is higher than the theoretical capacity of commercially used graphite anode (theoretical capacity = 372 mAh g^{-1}).[1] Lithium storage within these materials is based on the conversion of the original oxide into Li_2O and transition metal nanoparticles, the catalytic activity of which enables the reversible formation of the Li_2O, into which they are embedded. Among the various transition metal oxides, cobalt oxides exhibit excellent capacity values in the range of 700-900 mAh g^{-1} with good cyclability.[2] However, it has been reported that cobalt based oxides are not an ideal choice to replace graphite because of their high working voltage (~2.1 V versus Li/Li^+), cost, and toxicity.[3-4] Furthermore, iron oxide (Fe_3O_4) in this transition series also offers a high theoretical capacity of 926 mAh g^{-1}, considering the complete reversible formation of four Li_2O per formula unit.[5] Since Fe_3O_4 is naturally abundant and environmentally friendly, it has attracted increasing interest for scientific investigation. In spite of the lower cost and better safety of Fe-based oxides, their capacity retention remains a major drawback. This is due to the considerable volumetric expansion/contraction that occurs during the charging/discharging process, ultimately leading to pulverization of the electrode from the current collector, resulting in loss of electrical contact.[6-7] However, nanostructured Fe-based binary (AB_2O_4) oxides, especially ferrites, have recently been explored as anode materials in lithium ion batteries to improve cyclability. In addition, a major advantage of the AB_2O_4 type metal oxides is that the two transition elements (both A- and B-sites) make it feasible to adjust the energy density and working voltages by varying the transition metal content. Therefore, the theoretical capacity of this transition metal oxide (Fe_3O_4) can be further increased by replacing an iron atom with an element which itself can reversibly form an alloy with lithium, such as Zinc.[8] This would result in an enhanced theoretical capacity of 1000.5 mAh g^{-1} with a lower working voltage of ~1.5V, according to the reversible reaction involving nine lithium ions per formula unit of $ZnFe_2O_4$ ($ZnFe_2O_4 + 9\ Li^+ + 9e^- \rightarrow LiZn + 2Fe^0 + 4Li_2O$). It is interesting to observe that $ZnFe_2O_4$ generates high capacity since lithium ions form an alloy with Zn and de-alloy, while Fe and Zn react with Li_2O to absorb/release Li^+ ion during lithiation/delithiation. Thus, $ZnFe_2O_4$ implements both conversion and alloy/de-alloy reaction, simultaneously.[7] Similar to other high capacity transition metal oxides, $ZnFe_2O_4$ also shows rapid capacity fading during cycling and reduced capacity at high charge/discharge rates due to the large volume change induced electrode pulverization and its poor electrical conductivity. Therefore, $ZnFe_2O_4$ has been engineered into many different nanostructures to enhance their electrode performances.[7, 9-15] However, developing high performance $ZnFe_2O_4$ electrode material with both good cycling stability and high rate capability remains a considerable challenge.

Recently, graphene nanosheets have been considered as an ideal host to support nanosized Li-storage due to their intriguing properties such as excellent electrical conductivity, large surface area, high mechanical strength, and chemical stability. In addition, graphene nanosheets have also flexible porous texture, which could be helpful to reduce the substantial buffering against volume expansion/contraction during Li^+ ion insertion/extraction.[2]

However, in the present work, the $ZnFe_2O_4$/graphene nanocomposite was synthesized using a facile and cost-effective urea-assisted auto-combustion synthesis combined with subsequent annealing treatment at a low temperature of 600 ºC for 5 h under an N_2 atmosphere. Urea-assisted auto-combustion synthesis is an efficient and convenient method for preparing metal oxide nanoparticles at relatively low temperatures.[2, 16-18] This process produces sub-nanometer-size metal oxide nanoparticles using the self-generated heat of the reaction with a very short reaction time. The advantage of urea is that it can form stable complexes with metal ions that increase the solubility and prevent the selective precipitation of the metal ions during water removal.[2, 16-18] In addition, the oxides that form after combustion are generally composed of very fine particles with the desired stoichiometry linked together in a network structure. The sub-nanometer particles were randomly dispersed and anchored on the reduced graphene nanosheets during combustion. The obtained nanocomposite electrode exhibited high reversible capacity, better cycling stability, and more improved rate capability compared to pure $ZnFe_2O_4$ nanoparticle electrode.

2. Experimental

2.1. Preparation of graphene oxide and graphene nanosheets:

In a typical synthesis method, graphene oxide (GO) is first synthesized using the modified Hummers method[19] and the obtained GO colloidal suspension is maintained at room temperature for a long period of time. Second, the obtained GO is reduced to graphene nanosheets using the polyol-based reduction method. The detailed preparation procedure for the reduction of graphene nanosheets can be found in our previous papers.[20]

2.2. Materials Synthesis:

All chemicals used in the experiment were of analytical grade and used as received, without further purification. In a typical procedure, pure $ZnFe_2O_4$ and $ZnFe_2O_4$/graphene nanocomposite were synthesized by urea-assisted auto-combustion synthesis using starting materials of zinc nitrate hexahydrate [($Zn(NO_3)_2.6H_2O$, 98%, Sigma Aldrich], iron nitrate nonahydrate [$Fe(NO_3)_3.9H_2O$; 98% Junsei], and urea [NH_2CONH_2; 99% Sigma Aldrich]. The detailed synthesis procedure is shown in scheme 1. Briefly, the molar ratio of Zn/Fe was fixed at 1:2. Initially, both zinc nitrate and iron nitrate were dissolved in distilled water separately under continuous stirring at room temperature to obtain transparent solutions. Both solutions were then mixed together with a separately prepared aqueous solution of urea; the ratio between urea and nitrates was maintained at 25:12 to allow for controlled combustion (urea : zinc nitrate = 10 : 6 and urea : iron nitrate = 15 : 6).[18] At the same time, 10 wt% of the reduced graphene nanosheet was also added to the mixed solution to allow the nanoparticles to anchor on the graphene nanosheets. The obtained ternary mixed solution was evaporated on a hot plate using a magnetic stirrer at 350 ºC under continuous stirring to remove excess water. During the evaporation, the homogeneously mixed solution turned viscous, eventually becoming a gel. The formed gel slowly foamed, swelled, and finally burned on its own. In order to eliminate possible organic residues and to stabilize the microstructure of the $ZnFe_2O_4$/graphene nanocomposite, the as-synthesized powder was subsequently annealed at 600 ºC for 5 h in an N_2 atmosphere. For comparison, pure $ZnFe_2O_4$ nanoparticle was also synthesized under the same condition without the addition of graphene nanosheets. The overall combustion reactions are represented as follows:[18]

$$3Zn(NO_3)_2 + 6Fe(NO_3)_3 + 20NH_2CONH_2 + Graphene \rightarrow 3ZnFe_2O_4/graphene + 32N_2 + 40H_2O + 20CO_2 \qquad \text{(i)}$$

$$3Zn(NO_3)_2 + 6Fe(NO_3)_3 + 20NH_2CONH_2 \rightarrow 3ZnFe_2O_4 + 32N_2 + 40H_2O + 20CO_2 \qquad \text{(ii)}$$

In the urea-assisted auto-combustion synthesis, the nitrate ions act as the oxidizer, while the urea acts as the fuel. The reaction products are finely divided into the metal oxide and the evolved gases of N_2, CO_2, and H_2O. The excess urea also decomposes into ammonia and other gases.

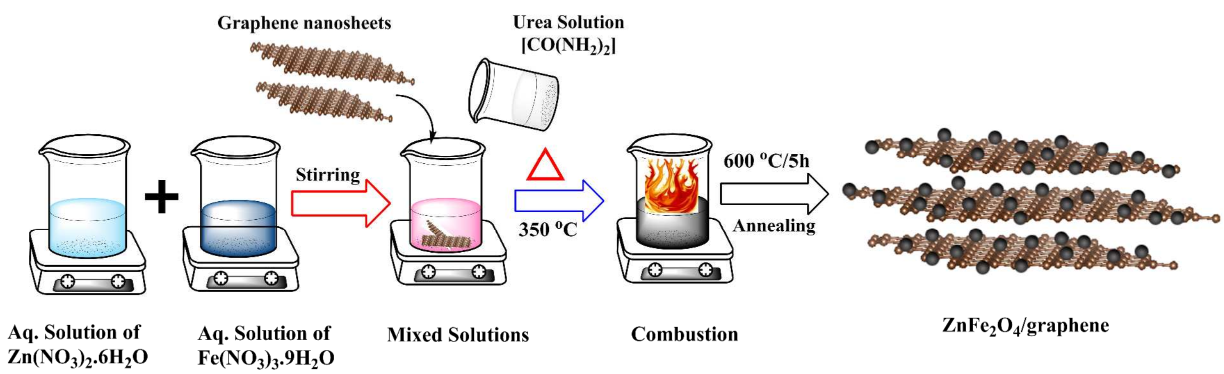

Scheme 1 Schematic illustration of the preparation of $ZnFe_2O_4$/graphene nanocomposite

2.3. Materials Characterization:

To investigate the crystal structures of the annealed pure $ZnFe_2O_4$ and $ZnFe_2O_4$/graphene powders, Synchrotron X-ray powder diffraction data was collected at the 9B high resolution powder diffraction beamline of the Pohang Light Source, Korea. Data was collected over the angular 2θ range of 10–80º. The incident X-rays were monochromatized to the wave length of 1.46470 Å using a double-bounce Si (111) monochromator. The surface morphology, particles size, and microstructures of the obtained products were observed using field-emission scanning electron microscopy (FE-SEM, S-4700 Hitachi) and field-emission transmission electron microscopy (FE-TEM, Philips Tecnai F20 at 200 kV, KBSI, Chonnam National University, South Korea). The carbon contents in both the annealed pure $ZnFe_2O_4$ and $ZnFe_2O_4$/graphene nanocomposite samples were determined by CHN elemental analysis using Flash-2000 Thermo Fisher. The Raman spectrum of the $ZnFe_2O_4$/graphene nanocomposite and as-prepared graphene nanosheets were conducted on a LabRam HR800 UV Raman microscope (Horiba Jobin-Yvon, France, KBSI, Gwangju Centre), using 514 nm (10 mW) laser excitation. The spectra was recorded in a range of 800−3000 cm^{-1} at room temperature with accumulated scans for an enhanced resolution.

2.4. Electrochemical measurements:

The electrochemical performance of pure $ZnFe_2O_4$ and $ZnFe_2O_4$/graphene nanocomposite were evaluated by using coin-type (CR-2032) half-cell assembled in an argon-filled glove box. The electrodes were prepared by mixing 70 wt.% active material, 20 wt.% Super P as a conducting agent, and 10 wt.% PVDF as a binder in N-methyl-2-pyrrolidinone (Sigma Aldrich) solvent to form a homogenous slurry. The slurry was coated on copper foil as a current collector using the doctor blade technique and dried at 100 ºC in a vacuum oven for 12 h. Subsequently, the coating was pressed between stainless still twin rollers to improve the adhesion between copper foil and active materials. The electrodes were cut into circular disks and assembled as half-cells in a glove box. Lithium metal was used as a counter electrode, Celgard 2400 was used as the separator, and 1 M solution of $LiPF_6$ dissolved in ethylene carbonate/dimethyl carbonate (EC:DMC = 1:1 by volume) was used as the electrolyte. Cyclic voltammetry (CV) measurement of the electrodes were performed between 0 to 3 V (versus Li^+/Li) using a Bio Logic Science instrument (VSP 1075) at a scan rate of 0.1 mV S^{-1}. Galvanostatic testing of the coin cells were conducted using a programmable battery tester over the potential range of 0.005-3.0 V vs. Li^+/Li (BTS-2004H, Nagano, Japan). Electrochemical impedance spectroscopy (EIS) measurement of the electrodes were also carried out on a Bio Logic Science Instrument (VSP 1075). Before the EIS measurements, both the electrodes were cycled for 5 cycles and then measured in the frequency range from 1 Hz to 100 kHz. A small ac signal of 5 mV was used to perturb the system throughout the tests.

3. Results and Discussion:

3.1. Crystal Structure and Morphology:

Fig. 1 (a) and (b) shows the synchrotron XRD patterns of pure $ZnFe_2O_4$ and $ZnFe_2O_4$/graphene nanocomposite samples, respectively, annealed at 600 ºC for 5 h under an N_2 atmosphere. As shown in Fig. 1 (a), all the major diffraction peaks from the XRD pattern of the pure $ZnFe_2O_4$ sample can be indexed to a standard cubic structure of the $ZnFe_2O_4$ spinel (JCPDS No. 82-1042). A similar XRD pattern was also obtained for the major diffraction peaks of the $ZnFe_2O_4$/graphene nanocomposite sample, as shown in Fig. 1 (b). However, typical diffraction peaks of graphene (002) were not observed in the XRD pattern of the $ZnFe_2O_4$/graphene nanocomposite sample. The absence of graphene peaks may be ascribed to the fact that the graphene nanosheets are completely coated with $ZnFe_2O_4$ nanoparticles and homogenously dispersed.[2] On the other hand, the pure $ZnFe_2O_4$ sample shows some small impurity peaks in the pattern (Fig. 1(a)), which are well matched with ZnO (JCPDS card no. 79-0205) and Fe_2O_3 (JCPDS card no. 89-0599) metal oxide peaks, whereas the

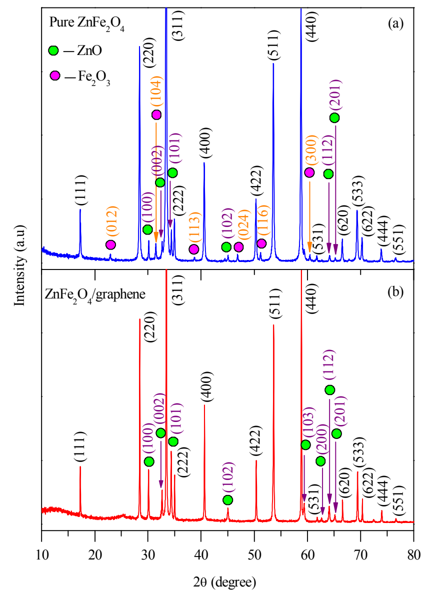

Fig. 1 Synchrotron X-ray diffraction patterns of (a) pure $ZnFe_2O_4$ and (b) $ZnFe_2O_4$/graphene nanocomposite sample

$ZnFe_2O_4$/graphene nanocomposite sample displays only ZnO peaks in the pattern as an impurity phase. The presence of the ZnO peaks in the nanocomposite sample is due to the decomposition of $ZnFe_2O_4$, which may have occurred due to the consumption of the reduced graphene nanosheets at elevated temperatures.[2]

The surface morphologies of the pure $ZnFe_2O_4$ and the $ZnFe_2O_4$/graphene nanocomposite samples were investigated using FE-SEM and FE-TEM. Fig. 2 (a) shows an FE-SEM image of the pure $ZnFe_2O_4$ sample. It can be seen that the $ZnFe_2O_4$ nanoparticles exhibit a spherical shape with almost uniform size distribution. Furthermore, the FE-TEM image shown in Fig. 2 (b) clearly confirms that the obtained pure $ZnFe_2O_4$ nanoparticles were severely agglomerated in the current combustion synthesis method. It is well-known that smaller primary nanoparticles aggregate into secondary particles, which is probably due to their extremely small dimensions and high surface energies. The large particles could lead to poor rate capabilities of $ZnFe_2O_4$ as anode materials for lithium-ion batteries because of the long diffusion path for both lithium–ion and electrons during the lithium-ion insertion/extraction process. A representative HR-TEM image of pure $ZnFe_2O_4$ nanoparticle is also shown in Fig. 2 (c). The lattice spacing measured from the fringe pattern are 2.57 Å and 2.45 Å, which correspond to the (311) and (222) planes, respectively, as observed from the XRD results. After being modified with graphene nanosheets, the typical structure and morphology of the $ZnFe_2O_4$/graphene nanocomposite were also studied using FE-SEM and FE-TEM. As shown in Fig. 2 (d), the $ZnFe_2O_4$/graphene nanocomposite consists of few nanosheets, resembling the general structure of conventional graphene nanosheets obtained by chemical reduction method. The image clearly shows that the small $ZnFe_2O_4$ nanoparticles were anchored on to the surface of graphene nanosheets. As depicted in the FE-TEM image (Fig. 2 (e)), it can be seen that the $ZnFe_2O_4$ nanoparticles uniformly anchored on the surface of the graphene nanosheets without serious aggregation.

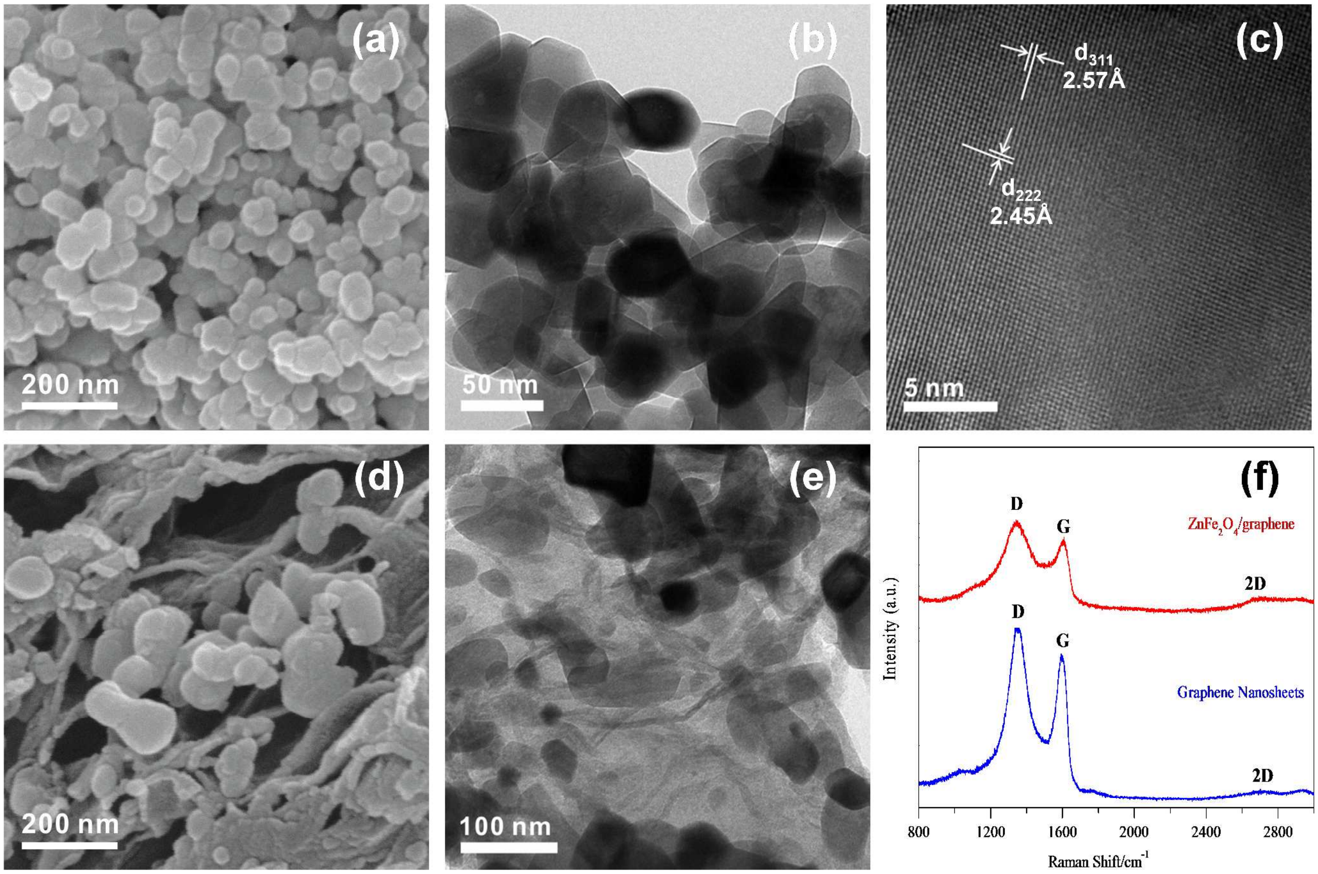

Fig. 2 FE-SEM and FE-TEM image of pure $ZnFe_2O_4$ nanoparticle (a and b) and $ZnFe_2O_4$/graphene nanocomposite (d and e) respectively. (c) The corresponding HR-TEM image of pure $ZnFe_2O_4$ nanoparticle. (f) Raman spectrum of $ZnFe_2O_4$/graphene nanocomposite and as-prepared graphene.

It is known that the interaction between the oxygen containing functional groups on the surface of graphene nanosheets and metal ions prevents the agglomeration of metal oxide nanoparticles to some extent.[21] The typical particle size of the pure $ZnFe_2O_4$ nanoparticle and $ZnFe_2O_4$/graphene nanocomposite samples are almost the same in the range of 25-50 nm in diameter. Raman spectroscopy is a powerful technique to characterize the existence and crystalline quality of graphene nanosheets. Fig. 2 (f) shows the Raman spectra of the $ZnFe_2O_4$/graphene nanocomposite and synthesized graphene nanosheet samples. The three typical peaks of 1348.4 cm^{-1}, 1608.8 cm^{-1} and 2664.9 cm^{-1} for $ZnFe_2O_4$/graphene and 1354.3 cm^{-1}, 1594.0 cm^{-1} and 2701.0 cm^{-1} for as-prepared graphene nanosheets are observed, which are associated with the D band, G band and 2D band, respectively. As reported in the literature,[2, 22] the D band is ascribed to sp^3 carbon and defects such as topological defects, dangling bonds, and vacancies, whereas the G band is attributed to ordered sp^2 carbons. The significant increase of I_D/I_G intensity ratio (1.22) of graphene nanosheets in comparison to nanocomposite sample (1.17), indicated the decrease of the size of the in-plane sp^2 domains and partially disordered crystal structure of graphene nanosheets.[22] A broad and weak 2D band is also observed, which is an implication of the disorder induced D band and sensitive to the number of layers. However, it is reasonable to suggest that the few layered graphene nanosheets with some defect is successfully obtained, which may be favorable towards the improvement of the electrochemical properties.[22] In addition, the observed reduction of the intensity ratio in the nanocomposite sample may be due to the presence of abundant defects of graphene nanosheets by polyol reduction although the increase in the size of the in-plane sp^2 domains.[23]

In addition, to know the accurate percentage of carbon in both the annealed samples, CHN analysis has been also performed. The percentage of carbon in the pure $ZnFe_2O_4$ nanoparticle and $ZnFe_2O_4$/graphene nanocomposite samples were found to be 0.13% and 9.6%, respectively.

3.2. Electrochemical performance:

Fig. 3 (a) and (b) illustrates the CV profiles of the pure $ZnFe_2O_4$ nanoparticle and the $ZnFe_2O_4$/graphene nanocomposite electrodes, respectively from the 1st to 5th cycles between 0 to 3.0

V at a scan rate of 0.1 mV s^{-1}. In the 1st cathodic scan, a minor peak and broad peak located at ~0.77 V and ~0.49 V, respectively for pure $ZnFe_2O_4$ nanoparticle electrode, whereas only one broad peak centered at 0.55 V for $ZnFe_2O_4$/graphene nanocomposite electrode are observed, which can be attributed to the reduction of Zn^{2+} and Fe^{3+} to Zn^0 and Fe^0, respectively and the formation of Li-Zn alloy accompanied with solid electrolyte interphase film (decomposition of the electrolyte).[15] On the first anodic potential sweep, a broad oxidation peak around 1.61 V is observed for both the samples and could be attributed to the oxidation of the metallic Zn and Fe into Zn^{2+} and Fe^{3+}, respectively. More importantly, the large decrease in the integrated area between the first cycle and the following cycles for both the samples was consistent with the relatively low initial Coulombic efficiency, indicating the capacity loss caused by electrolyte decomposition, and SEI film formation. After the first cycle, the reduction and oxidation peaks are slightly shifted and fixed at around 0.89 V and 0.95 V and 1.66 V and 1.65 V for the remaining cycles of both the electrodes, respectively, corresponding to the reversible conversion reaction between ZnO and Fe_2O_3. Remarkably, it can be seen that the peak intensity of the pure $ZnFe_2O_4$ nanoparticle electrode decreases with the subsequent scan numbers, which may be due to the poor electrical conductivity of the sample, whereas the higher reversibility of $ZnFe_2O_4$/graphene nanocomposite sample can be attributed to the incorporation of graphene nanosheets.

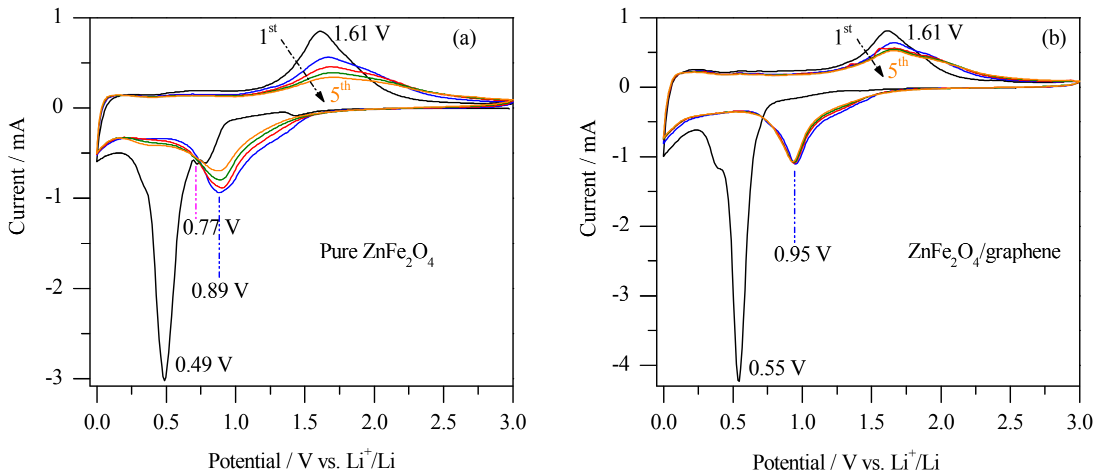

Fig. 3 Cyclic voltammograms of (a) pure $ZnFe_2O_4$ nanoparticle and (b) $ZnFe_2O_4$/graphene nanocomposite electrodes.

Fig. 4 (a) and (b) shows the charge/discharge curves of pure $ZnFe_2O_4$ and $ZnFe_2O_4$/graphene nanocomposite electrodes, respectively, for the 1st, 2nd and 5th cycles at 0.1 C [1 C = 1000.5 mA g^{-1}] in a potential range between 0.005-3.0 V vs. Li^+/Li. The specific capacity of the $ZnFe_2O_4$/graphene nanocomposite electrode is calculated based on the mass of the $ZnFe_2O_4$ only. For both samples, the first discharge-curve starts from the open circuit voltage (OCV~2.6 V) and shows a continuous decrease up to a deep discharge limit of ~0.005 V. It can be seen that a long discharge plateau was observed at ~0.8 V in the first discharge cycle of both electrodes, which can be speculated as the working voltage when crystal destruction occurs due to the conversion reaction of $ZnFe_2O_4$ into Zn, Fe, and Li_2O.[7, 9] In addition, both the electrodes also show a short voltage plateau near ~ 0.9 V, which may be due to the formation of $Li_xZnFe_2O_4$.[24] It can also be observed that the large discharge plateau disappears in the later cycles, indicating irreversible reactions occurred, such as electrolyte decomposition, or the formation of an SEI layer on the surface of the particles. For the first charge profile, a short steady increasing voltage plateau between 1.5-2.0 V is observed, which states that both the Zn and Fe metals can reversibly react with Li_2O to form metal oxides. The first discharge and charge capacities of the pure $ZnFe_2O_4$ nanoparticles are 1228.5 and 878.5 mAh g^{-1}, respectively, while those of $ZnFe_2O_4$/graphene nanocomposite are 1445.9 and 1002.5 mAh g^{-1}, respectively. For both the pure $ZnFe_2O_4$ and $ZnFe_2O_4$/graphene electrodes, the irreversible capacity during the first discharge process can be attributed to the incomplete conversion reaction and SEI layer formation at the electrode/electrolyte interface caused by the reduction of electrolyte. Since the second cycle, the $ZnFe_2O_4$/graphene nanocomposite electrode showed a more highly reversible behavior than the pure $ZnFe_2O_4$ electrode. Furthermore, the $ZnFe_2O_4$/graphene nanocomposite electrode retains a high reversible charge capacity of 908.6 mAh g^{-1} in the 5th cycle. The Coulombic efficiency rapidly increases from 69% in the first cycle to 97% in the fifth cycle, and then remains almost the same in the subsequent cycles (Fig. 4 (c)). In contrast, the reversible capacity of the pure $ZnFe_2O_4$ electrode rapidly decreases to 768.4 mAh g^{-1} with a low Coulombic efficiency of 94% after the fifth cycle. It is believed that the high reversibility of the nanocomposite electrode is due to its unique structure. Graphene nanosheets work as buffers to mitigate the large volume change of $ZnFe_2O_4$ in the charge/discharge process. It is well known that the excellent mechanical flexibility of graphene nanosheets can readily accommodate the large volume change associated with a conversion reaction electrode.

Fig. 4 (c) compares the cycle performance between the pure $ZnFe_2O_4$ electrode and $ZnFe_2O_4$/graphene nanocomposite electrode at a constant current rate of 0.1 C. It is obvious that the capacity maintaining for nanocomposite electrode is much better than that of the nanoparticle electrode. It can be seen that the charge capacity of pure $ZnFe_2O_4$ nanoparticle electrode reduces rapidly after 75 cycles and delivers only 128.2 mAh g^{-1}, which is only 15% of the reversible capacity for the first cycle, whereas the reversible capacity of $ZnFe_2O_4$/graphene nanocomposite electrode is stable and reaches a maximum of about 720.6 mAh g^{-1} after the same number of cycles. It should be noted that the obtained reversible capacity of the nanocomposite electrode is much higher than the theoretical capacity of commercially used graphite anode (372 mAh g^{-1}). Such a significant capacity fading for the pure $ZnFe_2O_4$ nanoparticle electrode may be due to its low intrinsic electrical conductivity, large volume expansion/contraction and the aggregation of the nanoparticles during the cycling process.[25] On the other hand, the improved cycling stability including both capacity and coulombic efficiency of the nanocomposite electrode is due to the existence of graphene nanosheets. The graphene nanosheets provide a highly conductive matrix for the diffusion of electrons and lithium ions during the lithium insertion and extraction reactions and improve the electronic conductivity, decrease the Ohmic loss, and further provide the electronic conduction pathway of the nanocomposite sample.

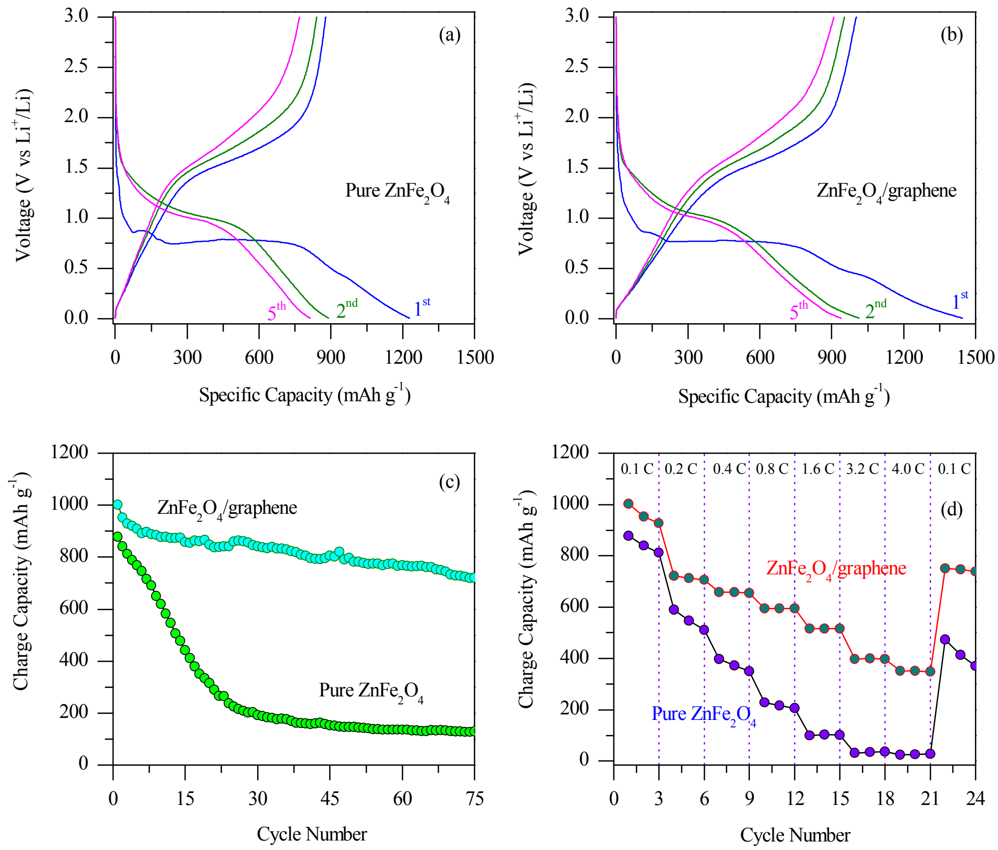

Fig. 4 Discharge/charge voltage profiles of (a) pure $ZnFe_2O_4$ nanoparticles and (b) $ZnFe_2O_4$/graphene nanocomposite electrodes. (c) Cycling performance at constant current rate of 0.1 C and (d) comparison of the rate capability at various current rates between 0.1 C to 4.0 C.

To further investigate the electrochemical performance of the pure $ZnFe_2O_4$ nanoparticle and $ZnFe_2O_4$/graphene nanocomposite electrodes, we evaluated the rate capability as shown in Fig. 4 (d). It can be seen that the charge capacities of the pure $ZnFe_2O_4$ nanoparticles decrease abruptly with increasing the current rates, whereas the $ZnFe_2O_4$/graphene nanocomposite decreases much slower at the same current rate. However, the $ZnFe_2O_4$/graphene nanocomposite exhibited excellent rate capability and delivered reversible charge capacities of 1002.5, 721.9, 658.8, 595.7, 516.7, 398.6, and 352.3 mAh g^{-1} at the current rates of 0.1 C, 0.2 C, 0.4 C, 0.8 C, 1.6 C, 3.2 C, and 4.0 C, respectively. It is worth noting that the obtained capacity of the nanocomposite electrode at the high current rate of 4.0 C is almost closer to the theoretical capacity of commercial graphite anode. In contrast, the capacities of pure $ZnFe_2O_4$ nanoparticle prepared under the same condition were only 878.5, 589.5, 397.6, 228.7, 99.4, 31.5, and 23.8 mAh g^{-1}, respectively. Hence, the result demonstrates that the structure of the nanocomposite is very stable, and the Li^+ ions insertion/extraction process is quite reversible even at the high current rates. It is believed that the $ZnFe_2O_4$/graphene nanocomposite not only suppresses the aggregation of $ZnFe_2O_4$ nanoparticles but also prevents the restacking of graphene nanosheets, resulting in a large electrode/electrolyte interface area. The large interface area not only provides more Li^+ insertion/extraction sites, but also facilitates fast Li^+ ion transfer between the electrode and electrolyte, thus leading to a large reversible capacity of the nanocomposite electrode. More importantly, the obtained electrochemical properties of designed $ZnFe_2O_4$/graphene nanocomposite electrode is comparable to those reported for pure $ZnFe_2O_4$ nanoparticle and their nanocomposite electrodes,[14-15, 26-28] but the synthesis strategy adopted in the present study is very cost-effective and simple compared to previous reports.

To further understand the enhanced electrochemical performance of $ZnFe_2O_4$/graphene nanocomposite, EIS measurements of pure $ZnFe_2O_4$ and $ZnFe_2O_4$/graphene electrodes were also performed. The typical EIS plots of pure $ZnFe_2O_4$ and $ZnFe_2O_4$/graphene electrodes are shown in Fig. 5. Both plots show a depressed semicircle in the high to intermediate frequencies region and a straight sloping line in the low frequencies region. Generally, the depressed semicircle represents charge-transfer resistance (R_{ct}) occurring at the electrode/electrolyte interface and the inclined line corresponds to the lithium-ion diffusion processes (Warburg impedance, W).[2] As can be seen from Fig. 5, the

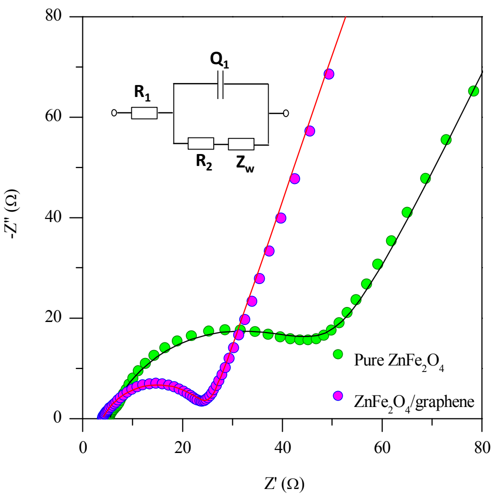

Fig. 5 Nyquist plots of pure $ZnFe_2O_4$ nanoparticle and $ZnFe_2O_4$/graphene nanocomposite electrodes.

impedance fitting was performed using EC-lab software and the corresponding equivalent circuit is also shown in the inset of the figure. The parameters R_1, R_2 and Z_w in the circuit correspond to the ohmic resistances of the electrolyte, Li^+ ion charge transfer and the Warburg impedance, respectively. However, the smaller the charge transfer resistance, the smaller the diameter of the semicircle. The results of fitting analysis clearly indicate that the R_2 value (14.39 Ω) for the $ZnFe_2O_4$/graphene nanocomposite electrode is smaller than the value of pure $ZnFe_2O_4$ nanoparticle electrode (25.76 Ω), indicating that the graphene nanosheets improve the electrical conductivity of nanocomposite electrode. Hence, author's believed that the high electrical conductivity of the graphene nanosheets could be maintained in the nanocomposite sample and holds the $ZnFe_2O_4$ nanoparticle tightly in the pores. This action prevents the $ZnFe_2O_4$ nanoparticle from aggregation and thereby enlarges the contact area between electrode and electrolyte. The high contact area makes it easy for much more Li^+ ions insertion/extraction at the same time, which eventually decreased the charge transfer resistances.

Additionally, post-cycling characterization of both the electrodes were performed to understand the volumetric expansion/contraction of $ZnFe_2O_4$ nanoparticles during charge/discharge cycling. Fig. 6 (a) and (b) shows the ex-situ FE-SEM images of pure $ZnFe_2O_4$ and $ZnFe_2O_4$/graphene nanocomposite electrodes, respectively, after 75 cycles. For doing ex-situ FE-SEM studies, the cycled electrode was initially dissociated from the cell in an argon filled glove box. The electrodes were then washed thoroughly with the solvent, dimethyl carbonate to remove the electrolyte. Then, they were dried at 80 ºC in a vacuum oven for overnight. For ex-situ FE-SEM studies, the electrode material is scraped off from the Cu-substrate and the powder is recovered inside the glove box.

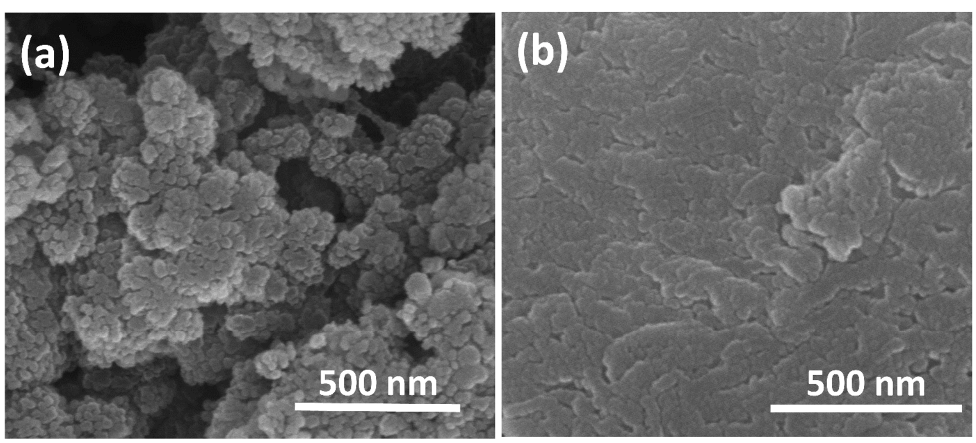

Fig. 6 Ex-situ FE-SEM images of cycled electrodes (a) pure $ZnFe_2O_4$ and (b) $ZnFe_2O_4$/graphene nanocomposite.

As shown in Fig. 6 (a), pure $ZnFe_2O_4$ nanoparticle electrode cracks severely and it seems that the nanoparticles are pulverized after 75 cycles. The structure destruction of $ZnFe_2O_4$ nanoparticle due to the cycling is responsible for its gradually decrease capacity. On the contrary, $ZnFe_2O_4$/graphene nanocomposite electrode preserves good geometric integrity without cracking. Therefore, it can be speculated that the active materials remain intact during cycling and thereby an excellent cycling stability of nanocomposite electrode. In addition, it is also reasonable to suggest that the introduction of graphene nanosheets provides buffer for the volume change of $ZnFe_2O_4$ nanoparticles and enhances its structure stability.

4. Conclusions

In conclusion, a $ZnFe_2O_4$/graphene nanocomposite was successfully synthesized by a rapid and facile urea-assisted auto-combustion synthesis and annealed at 600 ºC for 5 h under an N_2 atmosphere. The resultant nanocomposite reveals a unique morphology, in which the $ZnFe_2O_4$ nanoparticles with a range of 25-50 nm are homogeneously anchored on the surface of the graphene nanosheets. Furthermore, the electrochemical evaluation indicates that the $ZnFe_2O_4$/graphene nanocomposite is a promising candidate for lithium storage and shows a high reversible capacity, excellent cycling stability, and improved rate capability in comparison to the pure $ZnFe_2O_4$ nanoparticle electrode. The significantly improved electrochemical performance of nanocomposite electrode can be attributed to the fact that the $ZnFe_2O_4$ nanoparticles were bonded to the graphene nanosheets, which could greatly improve the intrinsic conductivity of $ZnFe_2O_4$ and effectively buffer the strain induced by lithiation.

Acknowledgments:

This work was supported by the Global Frontier R&D Program (2013-073298) of the Center for Hybrid Interface Materials (HIM) funded by the Ministry of Science, ICT & Future Planning. This research was also supported by the Ministry of Science, ICT & Future Planning (MSIP), Korea, under the Convergence Information Technology Research Center (C-ITRC) support program (NIPA-2013-H0301-13-1009) supervised by the National IT Industry Promotion Agency (NIPA).

Notes and references

Department of Materials Science and Engineering, Chonnam National University, 300 Yongbong-dong, Bukgu, Gwangju 500-757, Republic of Korea. Fax: +82-62-530-1699; Tel: +82-62-530-1703; E-mail: jaekook@chonnam.ac.kr

1 P. Poizot, S. Laruelle, S. Grugeon, L. Dupont and J. M. Tarascon, *Nature,* 2000, **407**, 496.
2 A.K. Rai, J. Gim, L.T. Anh and J. Kim, *Electrochim. Acta,* 2013, **100**, 63.
3 B. Guo, C. Li and Z.Y. Yuan, *J. Phys. Chem. C*, 2010, **114**, 12805.
4 R. Lauwerys and D. Lison, *Sci. Total Environ.,* 1994,**150**, 1.
5 D. Larcher, C. Masquelier, D. Bonnin, Y. Chabre, V. Masson, J.B. Leriche and J.M. Tarascon, *J. Electrochem. Soc.,* 2003, **150**, A133.
6 Z.S. Wu, W. Ren, L. Wen, L. Gao, J. Zhao, Z. Chen, G. Zhou, F. Li and H.M. Cheng, *ACS Nano,* 2010, **4**, 3187.
7 P.F. Teh, Y. Sharma, S.S. Pramana and M. Srinivasan, *J. Mater. Chem.,* 2011, **21**, 14999.
8 D. Bresser, E. Paillard, R. Kloepsch, S. Krueger, M. Fiedler, R. Schmitz, D. Baither, M. Winter and S. Passerini, *Adv. Energy Mater.,* 2013, **3**, 513.
9 Y. Sharma, N. Sharma, G.V.S. Rao and B.V.R. Chowdari, *Electrochim. Acta,* 2008, **53**, 2380.
10 Y.N. NuLi, Y.Q. Chu and Q.Z. Qin, *J. Electrochem. Soc.,* 2004, **151**, A1077.
11 X. Guo, X. Lu, X. Fang, Y. Mao, Z. Wang, L. Chen, X. Xu, H. Yang and Y. Liu, *Electrochem. Commun.,* 2010, **12**, 847.
12 Y. Deng, Q. Zhang, S. Tang, L. Zhang, S. Deng, Z. Shi and G. Chen, *Chem. Commun.,* 2011, **47**, 6828.
13 F. Mueller, D. Bresser, E. Paillard, M. Winter and S. Passerini, *J. Power Sources,* 2013, **236**, 87.
14 Y. Ding, Y. Yang and H. Shao, *Electrochim. Acta,* 2011, **56**, 9433.
15 J. Sui, C. Zhang, D. Hong, J. Li, Q. Cheng, Z. Li and W. Cai, *J. Mater. Chem.,* 2012, **22**, 13674.
16 A. Ringuede, J. A. Labrincha and J. R. Frade, *Solid Stae Ionics,* 2001, **141-142**, 549.
17 A.K. Rai, L.T. Anh, J. Gim, V. Mathew and J. Kim, *Electrochim. Acta,* 2013, **109**, 461.
18 A.K. Rai, J. Gim, T.V. Thi, D. Ahn, S.J. Cho and J. Kim, *J. Phys. Chem. C*, 2014, **118**, 11234.
19 W.S. Hummers and R.E. Offeman, *J. Am. Chem. Soc.,* 1958, **80**, 1339.
20 A.K. Rai, J. Gim, S. Kang, V. Mathew, L.T. Anh, J. Kang, J. Song, B.J. Paul and J. Kim, *Mater. Chem. Phys.,* 2012, **136**, 1044.
21 H.L. Wang, J.T. Robinson, G. Diankov and H. Dai, *J. Am. Chem. Soc.,* 2010, **132**, 3270.
22 K. Zhang, P. Han, L. Gu, L. Zhang, Z. Liu, Q. Kong, C. Zhang, S. Dong, Z. Zhang, J. Yao, H. Xu, G. Cui and L. Chen, *ACS Appl. Mater. Interfaces,* 2012, **4**, 658.
23 J. Qu, L. Shi, C. He, F. Gao, B. Li, Q. Zhou, H. Hu, G. Shao, X. Wang and J. Qiu, *Carbon,* 2014, **66**, 485.
24 N. Wang, H. Xu, L. Chen, X. Gu, J. Yang and Y. Qian, *J. Power Sources,* 2014, **247**, 163.
25 L. Yao, X. Hou, S. Hu, J. Wang, M. Li, C. Su, M.O. Tade, Z. Shao and X. Liu, *J. Power Sources,* 2014, **258**, 305.
26 L. Yao, X. Hou, S. Hua, X. Tang, X. Liu and Q. Ru, *J. Alloys Comp.,* 2014, **585**, 398.
27 H. Xu, X. Chen, L. Chen, L. Li, L. Xu, J. Yang and Y. Qian, *Int. J. Electrochem. Sci.,* 2012, **7**, 7976.
28 M. A Woo, T. W. Kim, I. Y. Kim and S. J. Hwang, *Solid State Ionics*, 2011, **182**, 91.